An E-Core Based Integrated Coupled Inductor for Interleaved Boost Converter

Abdul Basit Mirza, *Graduate Student Member, IEEE*, Asif Imran Emon, *Graduate Student Member, IEEE*, Sama Salehi Vala, *Graduate Student Member, IEEE*, and Fang Luo, *Senior Member, IEEE*

***Abstract*—Interleaving in a boost converter is beneficial for lowering input and output current ripples through ripple cancellation due to phase-shift between channel currents. However, interleaving does not affect the channel current ripple. The channel current comprises circulating Differential Mode (DM) current and Common Mode (CM) boost current, whose ripples constitute the total channel current ripple. Inverse coupling between channel inductors effectively lowers channel current ripple while maintaining the same input and output current ripples. However, with a single inverse coupled inductor, its leakage inductance, which serves as a boost inductor, depends on the winding arrangement and is challenging to balance in both channels. To overcome this, the inverse coupled inductor can be implemented as a cascade of inverse (DM inductance) and direct (CM inductance) coupled inductors. The DM and CM currents and their ripples then depend on CM and DM inductances, respectively. Nonetheless, this approach results in increased size and count of magnetic cores. In this paper, an Integrated Magnetic Structure (IMS), based on a gapped EE-core, is proposed that combines both CM and DM inductances in a single core. The CM and DM inductances are independent and depend on separate winding turns. A reluctance model is derived, and a design procedure is developed where core parameters are expressed in terms of converter parameters. Finally, the proposed IMS concept is validated through a 300 W, 100 V to 168 V prototype, switching at 70 kHz.**

***Index Terms*—CM and DM inductance, coupled inductor, EE-core, interleaved boost converter, integrated magnetic structure, schwarz-christoffel transformation.**

I. Introduction

TWO-PHASE interleaving in a simple boost converter has benefits like twice effective switching frequency, harmonic cancellation, better efficiency and increased power density [1]. It is also beneficial for the output filter capacitor. The Equivalent Series Resistance (ESR) of the tantalum capacitor is inversely proportional to the frequency of the switching current and interleaving can effectively reduce the filter capacitor size, loss and weight [2]. Further, the input current ripple is lower than the non-interleaved case due to the phase shift between the channel currents. However, the lower input current ripple is achieved through ripple cancellation of the channel ripples, the channel or inductor current ripple is still large if the inductance is small [1], [2].

Inverse coupling between channel inductors is proven effective in lowering channel current ripple while maintaining the same input and output current ripples [3], [4]. The channel current in an interleaved boost converter consists of CM and DM current components, which depend on the same channel inductance L. Assuming identical channels, the CM current in each channel is half of the input current, comprising DC and AC ripple components [5], [6], [7]. In contrast, the DM current is an AC circulating current between channels without DC bias. According to [8], the DM ripple component dominates the channel current ripple, which can be reduced by increasing L. Nonetheless, this is achieved at the cost of increased core volume/turns to accommodate increased ampere-turns (NI) due to CM current DC component, which also flows through the same L.

Through inverse coupling (Fig. 2), the CM and DM current ripples are decoupled and depend separately on leakage (CM) and mutual (DM) inductances, respectively [1], [6]. The DC magnetization produced by CM current in both windings cancels out, while the mutual DM inductance determines the DM ripple. However, the leakage CM inductance is winding orientation and core structure dependent, lowering flexibility in controlling the CM ripple. A cascaded inverse (L_{CM}) and direct coupled (L_{DM}) inductor realization of inverse coupled inductor is proposed and implemented in [8], which provides complete flexibility in controlling CM and DM ripples separately. The inductors L_{CM} and L_{DM} are built using U-U cores and cascaded together.

The inverse and direct coupled inductor implementation of inverse coupled inductor requires two separate cores, which increases the overall size and count of converter magnetics. Several approaches have been proposed in the literature for the miniaturization of magnetics by integrating both L_{CM} and L_{DM} in a single structure. Basic EE-core-based structures with channel windings on outer limbs are proposed in [9], [10], [11].

Manuscript received 30 October 2022; revised 13 January 2023 and 22 February 2023; accepted 8 March 2023. Date of publication 20 March 2023; date of current version 19 July 2023. Paper 2022-IPCC-1109.R2, presented at the 2021 IEEE Energy Conversion Congress and Exposition, Vancouver, BC, Canada, Oct. 10–14, and approved for publication in the IEEE Transactions on Industry Applications by the Industrial Power Converter Committee of the IEEE Industry Applications Society [DOI: 10.1109/ECCE47101.2021.9596045]. This work was supported in part by Oak Ridge National Laboratory (ORNL) funded through the Department of Energy (DOE) - Office of Electricity's (OE), Transformer Resilience and Advanced Components (TRAC), program led by the program manager Andre Pereira, and in part by the National Science Foundation (NSF) under Grant 1846917. *(Corresponding author: Abdul Basit Mirza.)*

The authors are with the Electrical and Computer Engineering, Stony Brook University, Stony Brook, NY 11794 USA (e-mail: abdulbasit.mirza@stonybrook.edu; asifimran.emon@stonybrook.edu; sama.salehivala@stonybrook.edu; fang.luo@stonybrook.edu).

Color versions of one or more figures in this article are available at https://doi.org/10.1109/TIA.2023.3258940.

Digital Object Identifier 10.1109/TIA.2023.3258940

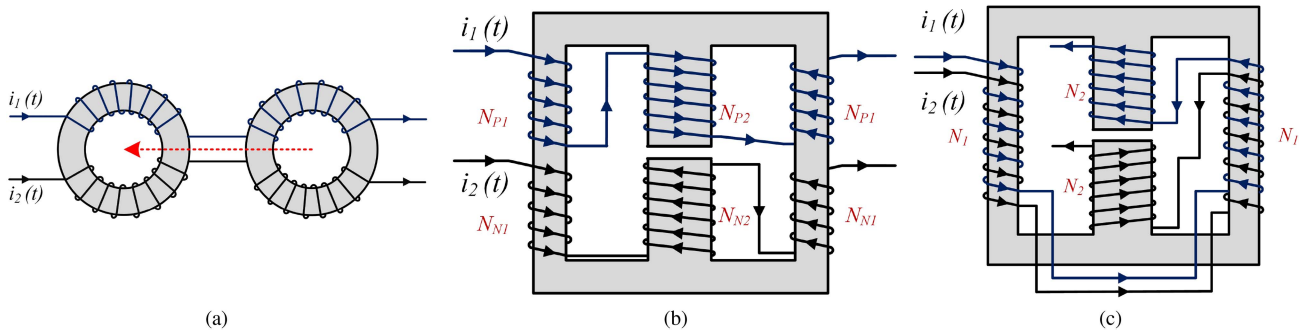

Fig. 1. IMSs for EMI filter proposed in literature. (a) Stacked Toroidal Structure [15]. (b) EE-core structure with center leg air-gap [16]. (c) EE-core structure with center leg air-gap and bifilar winding [17].

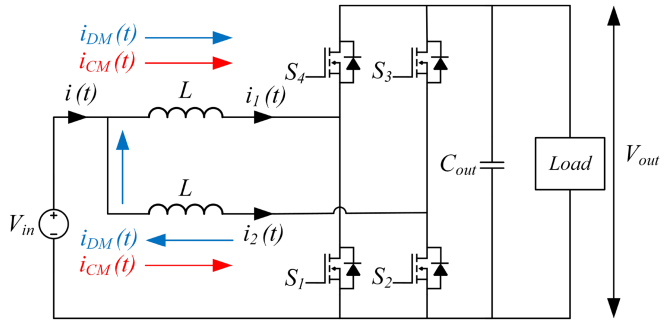

Fig. 2. Two-phase interleaved boost converter with inverse coupled inductor.

The air-gap is either provided in the outer legs [9], [10] or in all legs [11]. The structures are shown to provide better transient performance but the CM and DM inductances are not decoupled and cannot be controlled independently. Moreover, the core needs to be aligned precisely. For instance, the E and I cores in Fig. 2 in [9] connect through the center leg. Hence, gap-filling inside air-gaps is necessary to ensure mechanical stability and to prevent displacement between the two cores.

Similarly, an EIE-core-based integrated structure is proposed in [12]. The structure utilizes two air gaps for energy storage. It is shown that the total air-gap length required for the proposed structure is less than the EE-core structure; however, a detailed comparison is not provided. Further, the inductances L_{CM} and L_{DM} are not independent and cannot be controlled separately. Further, a CCTT-core-based magnetic structure, proposed in [13], is shown to be effective in lowering winding fringe loss. The associated near-field emission is also less compared with the EE structure. However, the structure requires custom-designed cores, which increases the design and fabrication costs. The CM and DM inductances are also not decoupled as in [9], [10], [11], [12].

The concept of integrating CM and DM inductances in a single structure for an interleaved boost converter is analogous to the structure of an integrated filter for Electromagnetic Interference (EMI) suppression in power converters. In the context of EMI, several structures have been proposed to combine L_{CM} and L_{DM}. An integration method using two toroidal cores is proposed in [14]. While the volume is reduced considerably, L_{CM} and L_{DM} are not independent and the structure suffers from uneven thermal distribution. The stacked toroidal structure (Fig. 1(a)) in [15] provides high DM inductance but the size is considerably large. Moreover, L_{DM} is shown to depend on the mutual inductance M between two toroids, but no expression is provided for M. Similarly, the first structure, based on E-core, presented in [16] has high-near field emission and L_{CM} and L_{DM} are dependent on the same turns. The third structure presented in [16] and [17] proposes a design in which L_{CM} and L_{DM} are decoupled and depend on different winding turns, a feature lacking in the integrated structures discussed above (Fig. 1(a)). Also, it is concluded in [16] that this structure has lower near-field emissions due to near magnetic field cancellation.

This paper draws an inference from IMSs proposed in [16], [17] for EMI suppression and extends it to an IMS design for a bi-directional two-phase interleaved boost converter [18]. At first, CM and DM modeling of an interleaved boost converter for both uncoupled and coupled configurations is discussed in Section II. A comparative study of converter performance for both inductor configurations in Section III follows this. The CM and DM modeling approach for an interleaved boost converter has yet to be discussed in detail in the existing literature. Although CM and DM current modeling approach has been used to design a Buck-Boost converter in [8], the underlying expressions for CM and DM current components differ from those for the interleaved boost converter.. The CM and DM modeling presented in Section II serves as a basis for the analysis of the proposed IMS. Section IV introduces the proposed IMS and presents analysis for deriving expressions for L_{CM} and L_{DM}, followed by a detailed discussion of the design procedure. In addition, Section IV also discusses the extension of the proposed IMS to multi-phase boost converters and an iterative approach for estimation of input current ripple. Lastly, Section V presents IMS concept validation and performance comparison on a hardware prototype.

II. Review of Uncoupled and Inverse Coupled Converter Design and Operation

Fig. 2 shows the schematic of a two-channel bidirectional interleaved boost converter. The channel inductors L can be uncoupled or inverse coupled with mutual inductance M. The

channel currents $i_1(t)$ and $i_2(t)$ comprises the following two components: Circulating DM current $i_{DM}(t)$ and Boost current $i_{CM}(t)$. This circulating current is an inherent feature of interleaving regardless of coupling between the channels. It is generated by the differential voltage, which is produced due to switching of lower switches S_1 and S_2. $i_{CM}(t)$ is the actual boost converter current which flows in same direction in both channels. The CM and DM currents $i_{CM}(t)$ and $i_{DM}(t)$ can be expressed in terms of channel currents $i_1(t)$ and $i_2(t)$ as

$$i_{CM}(t) = \frac{i_1(t) + i_2(t)}{2} \tag{1}$$

$$i_{DM}(t) = \frac{i_1(t) - i_2(t)}{2} \tag{2}$$

The expressions for input current ripple Δi, channel current ripple $\Delta i_1 = \Delta i_2$ can be derived in terms of CM and DM current components for both uncoupled and inverse coupled inductor configurations.

A. Uncoupled

The steady state waveforms of an uncoupled two-phase interleaved boost converter are shown in Fig. 3. For both duty cycle ranges $D < 0.5$ and $D > 0.5$, there are four different operating states. The switches in ON state are marked on top in Fig. 3.

The input current is twice of CM current $i(t) = 2i_{CM}(t)$. Similarly, the current ripples in $i_{CM}(t)$ and $i_{DM}(t)$, Δi_{CM} and Δi_{DM} are related to input current ripple and channel current ripple as: $\Delta i_{CM} = 0.5\Delta i$ and $\Delta i_{DM} = \Delta i_1 - \Delta i_{CM} = \Delta i_2 - \Delta i_{CM}$. Through analysis of the steady-state waveforms, following equations are obtained for Δi, $\Delta i_1 = \Delta i_2$ and Δi_{DM} for both $D < 0.5$ and $D > 0.5$.

1) $D < 0.5$:

$$\Delta i_{CM} = \frac{V_{in} D(1-2D)}{2(1-D)fL} \tag{3}$$

$$\Delta i_{DM} = \frac{V_{in} D}{2(1-D)fL} \tag{4}$$

$$\Delta i = \frac{V_{in} D(1-2D)}{(1-D)fL} \tag{5}$$

$$\Delta i_1 = \Delta i_2 = \Delta i_{CM} + \Delta i_{DM} = \frac{V_{in} D}{fL} \tag{6}$$

2) $D > 0.5$:

$$\Delta i_{CM} = \frac{V_{in}(2D-1)}{2Lf} \tag{7}$$

$$\Delta i_{DM} = \frac{V_{in}}{2Lf} \tag{8}$$

$$\Delta i = \frac{V_{in}(2D-1)}{fL} \tag{9}$$

$$\Delta i_1 = \Delta i_2 = \Delta i_{CM} + \Delta i_{DM} = \frac{V_{in} D}{fL} \tag{10}$$

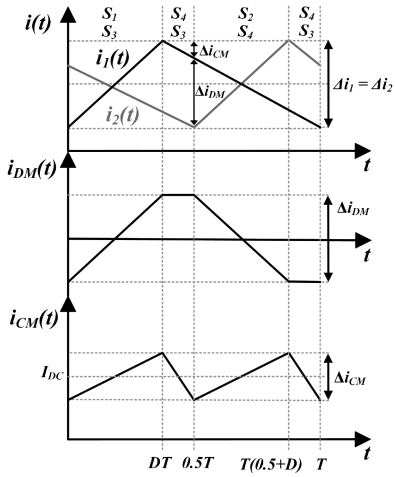

(a)

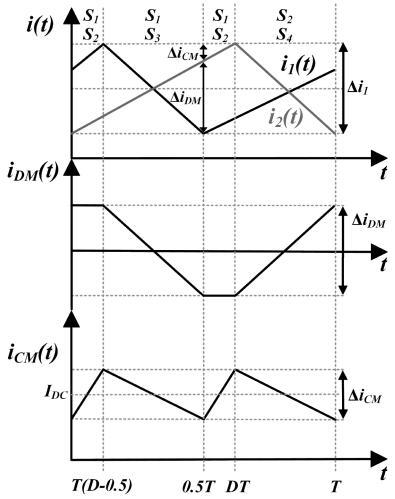

(b)

Fig. 3. Steady state waveforms of the converter with uncoupled inductor L. (a) $D < 0.5$. (b) $D > 0.5$.

B. Inverse Coupled

Inverse coupling results in different equivalent channel inductances for different switching states. The equivalent inductances depend on duty ratio D and on self and mutual inductances L and M [1]. This causes the channel currents to fall with different slopes, illustrated in Fig. 4. Similar to the uncoupled case, there are four different operating states and the switches in the ON state are marked on top in Fig. 4.

The CM current $i_{CM}(t)$ is dependent on the leakage inductance $L - M$ of the inverse coupled inductor. Nonetheless, the desired value of boost inductance $L - M$ is difficult to achieve as it depends on the layout of the winding and the structure of the core. To mitigate this issue, the inverse coupled inductor can be realized through a cascade of two separate inverse (L_{DM}) and direct (L_{CM}) coupled inductors as proposed in [2], [8]. Fig. 5 shows the transformation. Based on the direction of coupling, $i_{CM}(t)$ only sees L_{CM} and $i_{DM}(t)$ only sees L_{DM}. This implementation allows the desired value of boost inductance to

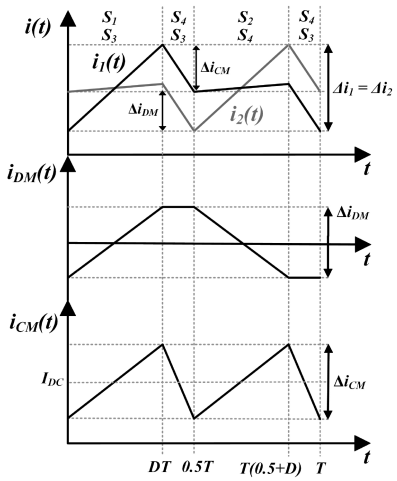

(a)

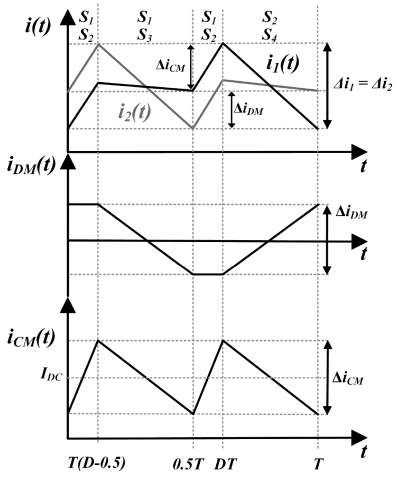

(b)

Fig. 4. Steady state waveforms of the converter with inverse-coupled inductors L_{CM} and L_{DM}. (a) $D < 0.5$. (b) $D > 0.5$.

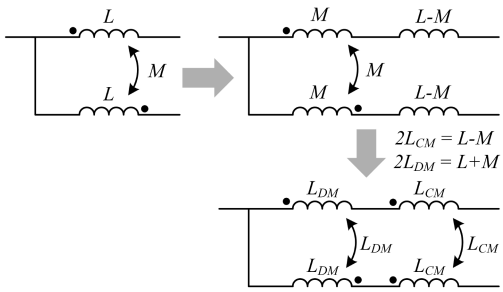

Fig. 5. Transformation of an inverse coupled inductor into inverse and direct coupled inductor.

be realized and to reap the benefit of inverse coupling, reducing the channel current ripple while maintaining the same transient response. Finally, the expressions for input current ripple Δi, channel current ripple $\Delta i_1 = \Delta i_2$ can be derived in terms of L_{CM} and L_{DM}.

1) $D < 0.5$:

$$\Delta i_{CM} = \frac{V_{in} D(1-2D)}{4(1-D)L_{CM} f} \tag{11}$$

$$\Delta i_{DM} = \Delta i_2 = \frac{V_{in} D}{4(1-D)L_{DM} f} \tag{12}$$

$$\Delta i = \frac{V_{in} D(1-2D)}{2(1-D) f L_{CM}} \tag{13}$$

$$\Delta i_1 = \Delta i_2 = \frac{V_{in} D(L_{DM}(1-2D) + L_{CM})}{4(1-D)L_{CM} L_{DM} f} \tag{14}$$

2) $D > 0.5$:

$$\Delta i_{CM} = \frac{V_{in}(2D-1)}{4L_{CM} f} \tag{15}$$

$$\Delta i_{DM} = \Delta i_2 = \frac{V_{in}}{4L_{DM} f} \tag{16}$$

$$\Delta i = \frac{V_{in}(2D-1)}{2 f L_{CM}} \tag{17}$$

$$\Delta i_1 = \Delta i_2 = \frac{V_{in}(L_{DM}(2D-1) + L_{CM})}{4L_{CM} L_{DM} f} \tag{18}$$

III. Comparative Study of Uncoupled and Inverse Coupled Configuration

Channel current ripple cancellation is the major benefit of the interleaving technique in a boost converter. However, interleaving only lowers the input current ripple Δi. The channel current ripples $\Delta i_1(t)$ and $\Delta i_2(t)$ are still significant. This results in increased core loss and winding loss due to greater harmonic content superimposed on top of DC current I_{DC} flowing through the channel. Inverse coupling lowers the steady-state channel current ripples, which improves converter performance and efficiency while maintaining the same transient response. Further, in terms of CM and DM currents, the decoupled L_{CM} and L_{DM} (Fig. 5) implementation of inverse coupled inductor in Fig. 2 makes CM and DM currents and their associated ripples to be controlled independently.

The proceeding analysis provides a performance comparison between uncoupled and inverse coupled inductor implementation, assuming equal Δi for both cases. This is achieved by setting L in (5) and (9) for the uncoupled case to twice of L_{CM} ($L = 2L_{CM}$).

A. Channel Current Ripple Comparison

According to (14) and (18) for $D < 0.5$ and $D > 0.5$, $\Delta i_1(t)$ and $\Delta i_2(t)$ for inverse coupling depends on both L_{CM} and L_{DM}, whereas it only depends on $L = 2L_{CM}$ for the uncoupled case in (6). By defining $\alpha = L_{CM}/L_{DM}$ and manipulating (14) and (18) to accommodate α, a channel current ripple ratio $\Delta r_{1,2}(D, \alpha)$ can be derived. The ratio depends on duty cycle D and α. Further it can be used to compare relative magnitude of channel current ripple for inverse coupled inductor ($\Delta i_{1,2(ic)}$) to

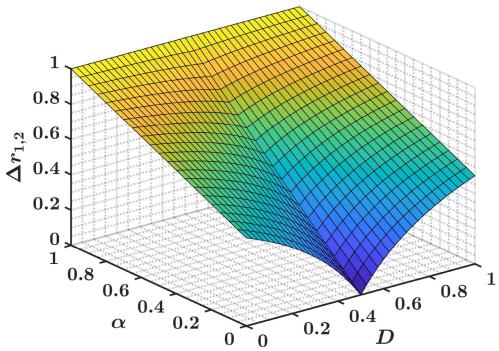

Fig. 6. Variation of $\Delta r_{1,2}$ with D and α.

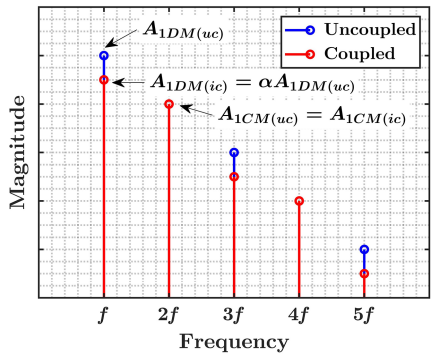

Fig. 7. Uncoupled and inverse coupled configuration harmonic content comparison.

that of uncoupled inductor ($\Delta i_{1,2(uc)}$).

$$\Delta r_{1,2}(D,\alpha) = \frac{\Delta i_{1,2(ic)}}{\Delta i_{1,2(uc)}} \tag{19}$$

The variation of $\Delta r_{1,2}(D,\alpha)$ with both D and α is illustrated in Fig. 6. The ratio equals 1 for $\alpha = 1$ for whole range of D. This is due the fact that for $\alpha = 1$ or $L_{CM} = L_{DM}$, ripple current expressions (14) and (18) reduce to (6). Further, the ratio drops non linearly for $\alpha < 1$, with minimum value at $D = 0.5$. This shows that inverse coupled implementation with $L_{DM} > L_{CM}$ is effective in lowering channel current ripple, while maintaining the same input current ripple. This also lowers the harmonic content in channel current, which is explained in the next subsection.

B. Harmonic Comparison

The channel currents $i_1(t)$ and $i_2(t)$ in Figs. 3 and 4 can be decomposed into DC component and switching frequency harmonics through Fourier series analysis. The magnitude of switching harmonics is critical as the harmonics are the driving factor for core loss and high AC resistance loss in windings due to skin effect. The channel currents are composed of $i_{CM}(t)$ and $i_{DM}(t)$ components. From (1) and (2), the channel currents are related to $i_{CM}(t)$ and $i_{DM}(t)$ as: $i_1(t) = i_{CM}(t) + i_{DM}(t)$ and $i_2(t) = i_{CM}(t) - i_{DM}(t)$. Hence, the Fourier series for $i_1(t)$ and $i_2(t)$ can be expressed as the sum or difference of the fourier series of $i_{CM}(t)$ and $i_{DM}(t)$. The CM and DM current fourier series with $\omega = 2\pi f$ can be expressed as follows (Appendix A).

1) Uncoupled:

$$i_{CM}(t) = I_{DC} + \sum_{n=1}^{\infty} \underbrace{\frac{2V_{in}}{L} g(D,f,2n)}_{A_{nCM(uc)}} cos(2n\omega t) \tag{20}$$

$$i_{DM}(t) = \sum_{n=1,3,5..}^{\infty} \underbrace{\frac{4V_{in}}{L} h(D,f,n)}_{A_{nDM(uc)}} cos(n\omega t) \tag{21}$$

2) Inverse Coupled:

$$i_{CM}(t) = I_{DC} + \sum_{n=1}^{\infty} \underbrace{\frac{V_{in}}{L_{CM}} g(D,f,2n)}_{A_{nCM(ic)}} cos(2n\omega t) \tag{22}$$

$$i_{DM}(t) = \sum_{n=1,3,5..}^{\infty} \underbrace{\frac{2V_{in}}{L_{DM}} h(D,f,n)}_{A_{nDM(ic)}} cos(n\omega t) \tag{23}$$

$g(D,f,n)$ and $h(D,f,n)$ are amplitude scaling factors, which depends on duty cycle D, switching frequency f and harmonic n. Further, $i_{CM}(t)$ fundamental component frequency is $2f$, due to interleaving, which is also evident in Fig. 3 and 4, respectively. On the other hand, $i_{DM}(t)$ only comprises odd harmonics of switching frequency f. Hence, the first harmonic in channel current at f is contributed solely from $i_{DM}(t)$.

For equal input current ripple Δi for both inverse and uncoupled ($L = 2L_{CM}$) inductor implementation, the CM current harmonic amplitude ratio $A_{nCM(ic)}/A_{nCM(uc)}$ is always unity for all D. However, in case of DM current, the $A_{nDM(ic)}/A_{nDM(uc)}$ ratio equals $\alpha = L_{CM}/L_{DM}$ or $A_{nDM(ic)} = \alpha A_{nDM(uc)}$. Hence for $\alpha < 1$, DM current harmonic content (including fundamental) for the inverse coupled case is always lower than the uncoupled case as illustrated in Fig. 7. This is results in lower core and winding loss while having the same Δi.

C. Power Semiconductor Loss Comparison

In a bi-directional interleaved boost converter, the diode in the top position in each phase-leg is replaced with a switch to achieve bidirectional current flow (Fig. 2). The total loss incurred by each switch is the sum of conduction loss P_{co} and switching loss P_{sw}. P_{co} affects the heavy-load efficiency whereas P_{sw} impacts light-load efficiency of the converter. The expressions for P_{sw} and P_{co} for top and bottom devices, using the converter waveforms in Figs. 3 and 4, can be derived as follows [19]

1) Bottom Switch:

$$P_{sw} = \frac{V_o f}{2}((I_{DC} - \Delta i_{1,2})T_{ON} + (I_{DC} + \Delta i_{1,2})T_{OFF}) \tag{24}$$

$$P_{co} = \frac{1}{T}\int_0^{DT} Rds_{on} i_{1,2}^2(\tau)\, d\tau \tag{25}$$

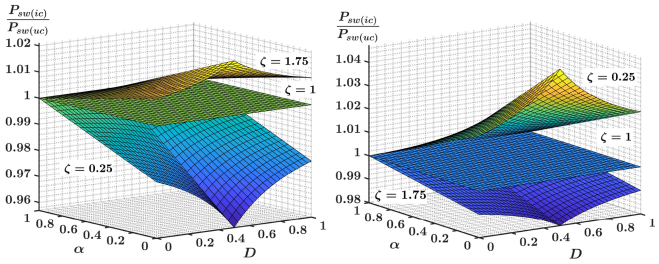

Fig. 8. Inverse coupled configuration normalized switching loss ($P_{sw(ic)}/P_{sw(uc)}$) variation with D, α, ζ and $\kappa = 0.15$. (a) Bottom device. (b) Top device.

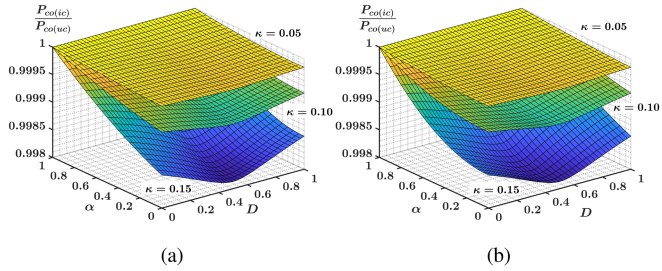

Fig. 9. Inverse coupled configuration normalized conduction loss ($P_{co(ic)}/P_{co(uc)}$) variation with D, α and κ. (a) Bottom device. (b) Top device.

2) Top Switch:

$$P_{sw} = \frac{V_o f}{2}((I_{DC} + \Delta i_{1,2})T_{ON} + (I_{DC} - \Delta i_{1,2})T_{OFF}) \tag{26}$$

$$P_{co} = \frac{1}{T}\int_{DT}^{T} Rds_{on} i_{1,2}^2(\tau)\, d\tau \tag{27}$$

T_{ON} and T_{OFF} represent the turn-ON and turn-OFF transient time duration for the switches $S_1 - S_4$. The loss expressions (24)–(27) show dependence on both channel currents $i_{1,2}(t)$ and their ripples $\Delta i_{1,2}$, which differ for uncoupled and inverse coupled configurations.

For intuitive comparison, the losses for the inverse coupled configuration can be normalized with losses for uncoupled configuration. Assuming same device parameters such as Rds_{on} and by turn-ON to turn-OFF time ratio $\zeta = T_{ON}/T_{OFF}$ and equal Δi for both inductor configurations, following normalized loss expressions are obtained (Appendix B):

$$\frac{P_{sw(ic)b,t}}{P_{sw(uc)b,t}} = M_{b,t}(D, \alpha, \zeta, \kappa) \tag{28}$$

$$\frac{P_{co(ic)b,t}}{P_{co(uc)b,t}} = N_{b,t}(D, \alpha, \kappa) \tag{29}$$

The subscripts b and t denote the bottom and top devices, respectively. α implies L_{CM}/L_{DM}. Similarly, $\kappa = \Delta i_{1,2}/I_{DC}$, lying within (0,1), represents the ratio of channel current ripple to its DC component (Fig. 3 and 4).

Fig. 8 shows the variation of normalized switching loss with D and α for three values of ζ and $\kappa = 0.15$ for both bottom and top switches using (28). The switching loss shows a similar trend to the inductor current ripple ratio plot in Fig. 11. For $\zeta < 1$, the normalized switching loss for the bottom device is upper bounded by 1, while it is lower bounded by 1 for the top device. The trend is the opposite for $\zeta > 1$. However, the total sum of normalized bottom and top device switching loss equals 2, implying that the net switching loss for uncoupled and inverse coupled configuration is the same. The total switching loss could be lowered if the bottom device has $\zeta < 1$ while the top switch has $\zeta > 1$.

The conduction loss variation with D and α for three values of κ is presented in Fig. 9. The conduction loss is upper bounded by 1 for all values of κ for both switches. However, compared with switching loss, the change (drop) in normalized conduction loss is insignificant with a decrease in α. This could be further supported by the fact that DC current component I_{DC} far dominates the conduction loss [19], which is the same for both inductor configurations.

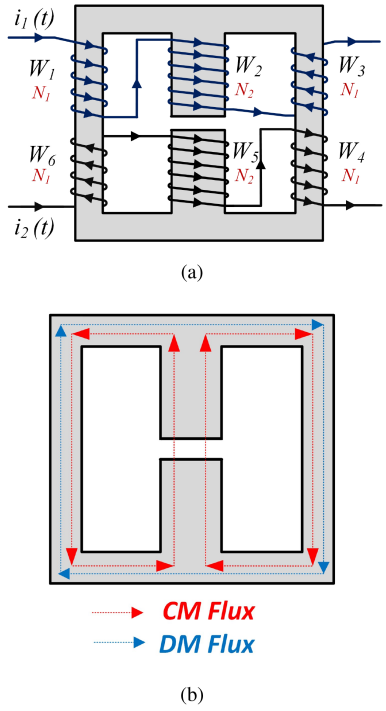

Fig. 10. Proposed integrated magnetic structure for two-phase interleaved boost converter with coupled inductor. (a) Winding layout. (b) Flux distribution.

IV. Integrated Magnetic Structure

The inverse and direct-coupled implementation of the main inverse coupled inductor in Fig. 5 decouples the CM and DM inductances. With L_{CM} and L_{DM} decoupled, the desired value of channel current ripple $\Delta i_1 = \Delta i_2$ and input current ripple Δi can be achieved. However, this implementation still results in the same number of inductor cores as for the uncoupled case, which calls for decoupled integration of both L_{CM} and L_{DM} in a single structure.

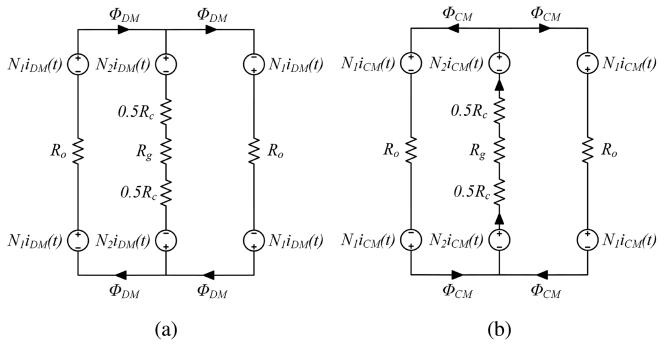

Fig. 11. Magnetic equivalent circuits for the proposed structure. (a) Differential Mode. (b) Common Mode.

The third EE-core structure for EMI filter with air-gap in the middle leg presented in [16] and [17] decouples L_{CM} and L_{DM}. The structure also has lower near-field emission due to near magnetic field cancellation and L_{CM} is much greater than L_{DM} due to low reluctance in CM flux path. According to [8], in an interleaved boost converter, L_{DM} is considerably greater than L_{CM}. The structure can be extended to inverse and direct-coupled structure (Fig. 5) to achieve miniaturization of magnetics for a two-phase interleaved boost converter in a single unified structure by interchanging the CM and DM flux paths (Fig. 10). This results in a significant value of L_{DM} with lower Equivalent Parasitic Capacitance (EPC) as the hardware results in the next section show. Fig. 10(b)) illustrates the flux distribution of CM and DM fluxes; the CM flux has a high reluctance air-gap in its path to prevent core saturation. The DM flux path has low reluctance and its direction alternates every half cycle.

Fig. 11 shows the equivalent magnetic circuits for DM and CM currents. R_o is the reluctance of the outer core, comprising the outer limb and half yoke from top and bottom. R_c is the total reluctance of the center limb excluding air-gap. Finally, R_g is the air-gap reluctance. The reason for separating R_c and R_g in Fig. 11 is the fringing effect, which causes the air-gap effective area to be larger than that of the center limb. An accurate air-gap R_g estimation approach using [20] is discussed in the proceeding section.

The center leg windings (W_2 and W_5) with N_2 turns are responsible for the CM inductance as the flux produced by the CM current in the center leg is in the same direction. The flux produced by the side limb windings (W_1, W_3, W_4 and W_6) with N_1 turns due to CM currents gets cancelled. On the other hand, the side limb windings with N_1 turns are responsible for DM inductance as the flux produced by DM current gets added, while the flux produced by the center leg windings with N_2 turns gets canceled. This leads to decoupling between L_{CM} and L_{DM} and these inductances depend on separate winding turns N_1 and N_2, respectively.

The six windings W_1–W_6 individually couple with each other with coupling factor k_{ij} between W_i and W_j. This results in a 6×6 coupling matrix k (30), which is symmetric ($k_{ij} = k_{ji}$) with all diagonal entries (k_{ii}) equal to 1. Hence, there are 15 matrix elements ($k_{ij} = k_{ji}$) that need to be determined to define (30) fully.

$$k = \begin{bmatrix} k_{11} & k_{12} & k_{13} & k_{14} & k_{15} & k_{16} \\ k_{21} & k_{22} & k_{23} & k_{24} & k_{25} & k_{26} \\ k_{31} & k_{32} & k_{33} & k_{34} & k_{35} & k_{36} \\ k_{41} & k_{42} & k_{43} & k_{44} & k_{45} & k_{46} \\ k_{51} & k_{52} & k_{53} & k_{54} & k_{55} & k_{56} \\ k_{61} & k_{62} & k_{63} & k_{64} & k_{65} & k_{66} \end{bmatrix} \tag{30}$$

$$k_c = \sqrt{\frac{R_o}{2(R_o + R_c + R_g)}} \tag{31}$$

$$k_o = \frac{R_c + R_g}{R_o + R_c + R_g} \tag{32}$$

A close observation of magnetic circuits in Fig. 11 reveals that the flux produced by top/bottom winding in each leg ideally fully links to the bottom/top winding in that leg or $k_{16} = k_{61} = k_{34} = k_{43} = k_{25} = k_{52} = 1$. The remaining matrix elements comprise two distinct coupling factors k_c and k_o, expressed in (31) and (32), to define k fully. k_c represents the coupling between outer leg winding (W_1, W_3, W_4, W_6) and center limb winding (W_2, W_5). k_o constitutes for the coupling between outer leg winding on one side (W_1, W_6) to the opposite side (W_3, W_4). The final coupling matrix k hence can be expressed as

$$k = \begin{bmatrix} 1 & k_c & k_o & k_o & k_c & 1 \\ k_c & 1 & k_c & k_c & 1 & k_c \\ k_o & k_c & 1 & 1 & k_c & k_o \\ k_o & k_c & 1 & 1 & k_c & k_o \\ k_c & 1 & k_c & k_c & 1 & k_c \\ 1 & k_c & k_o & k_o & k_c & 1 \end{bmatrix} \tag{33}$$

A. Derivation of L_{CM} and L_{DM}

According to Fig. 10(a), each channel comprises three windings connected in series. For instance, for channel carrying $i_1(t)$, the windings W_1, W_2 and W_3 are connected in series. The total equivalent winding voltage $v(t)_{eq1}$ for channel 1 can be expressed as sum of voltages across each of these windings (W_1, W_2 and W_3) (34).

$$v_{eq1}(t) = v_{w1}(t) + v_{w2}(t) + v_{w3}(t) \tag{34}$$

The expressions for L_{CM} and L_{DM} therefore can be derived by expanding (34) and collecting self (L_{ii}) and mutual (M_{ij}) inductance terms for CM and DM magnetic circuits in Fig. 11 separately. The mutual inductance M_{ij} can be computed using the self inductances L_{ii} and L_{jj} and the coupling factor k_{ij} (35).

$$M_{ij} = k_{ij}\sqrt{L_{ii}L_{jj}} \tag{35}$$

The proceeding subsection shows derivation of L_{CM} and L_{DM} using channel 1 as a reference. The same result can be obtained by using winding arrangement for channel 2, carrying $i_2(t)$.

1) L_{CM}:

$$v_{w1}(t) = \underbrace{(L_{11} - M_{12} + M_{13} - M_{14} - M_{15} - M_{16})}_{-2\left(\frac{0.5N_1N_2}{R_c+R_g+0.5R_o}\right)} i'_{CM}(t)$$

$$v_{w2}(t) = \underbrace{(L_{22} - M_{21} + M_{23} - M_{24} + M_{25} + M_{26})}_{2\left(\frac{N_2^2}{R_c+R_g+0.5R_o}\right)} i'_{CM}(t)$$

$$v_{w3}(t) = \underbrace{(L_{33} + M_{31} + M_{32} - M_{34} + M_{35} - M_{36})}_{2\left(\frac{0.5N_1N_2}{R_c+R_g+0.5R_o}\right)} i'_{CM}(t)$$

$$v_{eq1}(t) = 2\left(\frac{N_2^2}{R_c + R_g + 0.5R_o}\right) i'_{CM}(t) = 2L_{CM} i'_{CM}(t)$$

$$L_{CM} = \frac{N_2^2}{(R_c + R_g + 0.5R_o)} \tag{36}$$

2) L_{DM}:

$$v_{w1}(t) = \underbrace{(L_{11} - M_{12} + M_{13} + M_{14} + M_{15} + M_{16})}_{2\frac{N_1^2}{R_o}} i'_{DM}(t)$$

$$v_{w2}(t) = \underbrace{(L_{22} - M_{21} + M_{23} + M_{24} - M_{25} - M_{26})}_{0} i'_{DM}(t)$$

$$v_{w3}(t) = \underbrace{(L_{33} + M_{31} + M_{32} + M_{34} - M_{35} + M_{36})}_{2\frac{N_1^2}{R_o}} i'_{DM}(t)$$

$$v_{eq1}(t) = 2\left(\frac{2N_1^2}{R_o}\right) i'_{DM}(t) = 2L_{DM} i'_{DM}(t)$$

$$L_{DM} = \frac{2N_1^2}{R_o} \tag{37}$$

B. Influence of Air-Gap

The design of air-gap in gapped structure is critical as the reluctance R_g of air-gap is much larger than the reluctances of the core. R_g hence dominates the inductance whose flux passes through the air-gap, which is L_{CM} in the proposed IMS. The reluctance of an air-gap with gap length l_g and cross-sectional area A_g can be calculated as

$$R_g = \frac{l_g}{\mu_o A_g} \tag{38}$$

Ideally, A_g should be equal to A_c, which is the cross-sectional area of the core where the air-gap is situated. However, when the magnetic field lines pass through an air gap, they tend to spread out due to discontinuity introduced by the air-gap known as flux fringing [21]. Flux fringing causes A_g to be higher, eventually leading to increased inductance and flux density in the core [22], [23]. Further, it leads to eddy current loss in windings covering enclosing the air-gap. However, in the proposed structure, no winding covers the air-gap. Moreover, if the distance between winding edge on the core leg and air-gap edge is greater than twice of the air-gap, the losses due to fringing at air-gap are negligible and can be ignored [24].

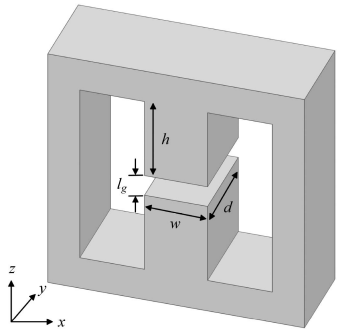

Fig. 12. 3D core geometry with labelled dimensions related to Schwarz-Christoffel transformation.

Several methods have been reported in the literature to estimate and compensate fringing effect in the design of air-gapped inductors. One conventional approach is to iteratively change the number of turns experimentally for a specific air gap length l_g until the desired inductance value is reached. The approach, albeit simpler, is time-consuming and ignores the effect of fringing on flux density [21]. Further, some closed-form models have been proposed to estimate R_g on paper without tweaking the number of turns. The most common closed-form model is the generic fringing factor F proposed by McLyman's equation in [22], [23] for C and E cores. F is the ratio of actual air-gap cross-sectional area A_g to core cross-sectional area A_c. McLyman's equation is limited to small air gaps and does not differentiate between air gaps with a rectangular or round cross-section. A more simplified closed-form approach is proposed in [25], [26]. The concept is to increase each edge of the gap cross-section by lg having perimeter p_c. The resulting F comes out to be $1 + l_g(0.5p_c) + l_g^2$, which is a quadratic equation. For small and large l_g, the approach is shown to under and over estimate A_g respectively [21].

In [20], [27], a capacitance to reluctance analogy, based of Schwarz-Christoffel transformation, is used to develop an analytical expression for air-gap reluctance estimation. The method is systematic and is shown to be accurate in estimating R_g, with a maximum of 5% deviation between calculated and measured inductance value [27]. Based on this, the Schwarz-Christoffel transformation approach in [27] is chosen for the estimation of R_g for the proposed IMS.

In the Schwarz-Christoffel transformation method, the air-gap 3D geometry is decomposed into basic 2D geometries to represent the front and side faces of the air-gap. Fig. 12 shows the 3D geometry of the proposed magnetic structure. The two 2D distinct geometries for the air-gap are in xz plane (x direction) and yz plane (y direction). w and d represent the width and depths of the air-gap, respectively. h is the inner height of the core leg. The 2D reluctance per-unit length, incorporating fringe effects, for x and y direction is related to core dimensions as follows [20], [27]

$$R'_x = \frac{1}{\mu_o\left(\frac{w}{l_g} + \frac{2}{\pi}\left(1 + ln\frac{\pi h}{2l_g}\right)\right)} \tag{39}$$

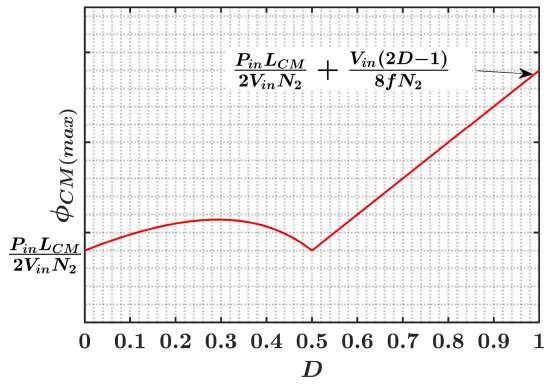

(a)

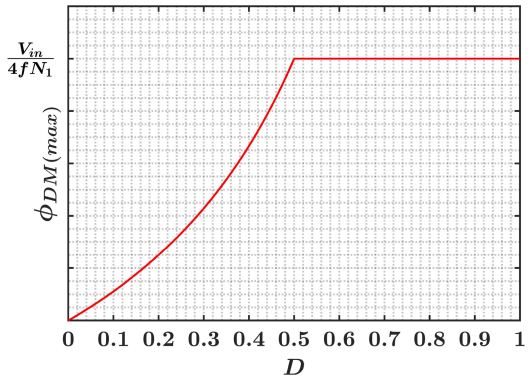

(b)

Fig. 13. Variation of maximum core flux components with duty cycle D. (a) CM. (b) DM.

$$R'_y = \frac{1}{\mu_o\left(\frac{d}{l_g} + \frac{2}{\pi}\left(1 + ln\frac{\pi h}{2l_g}\right)\right)} \tag{40}$$

Similarly, the 2D reluctance per-unit length, neglecting the fringing effects, can be computed as

$$R_x = \frac{l_g}{\mu_o w} \tag{41}$$

$$R_y = \frac{l_g}{\mu_o d} \tag{42}$$

The corrected air-gap reluctance R'_g could then be estimated with (38) and (39)–(42). Finally, R_g in (31)–(32) and (36)–(37) can be replaced with R'_g, to yield accurate value of inductance and core saturation current.

$$R'_g = \left(\frac{R'_x R'_y}{R_x R_y}\right) R_g = \sigma R_g \tag{43}$$

C. Flux Distribution and Core Saturation

The design of the proposed structure involves computing the number of turns N_1 and N_2, while ensuring that the core remains unsaturated. The DM inductance depends on the reluctance of the outer core, which is a known core parameter. Hence, for a desired value of L_{DM}, the required number of turns N_1 can be computed from (37). Further, N_2 for L_{CM} needs to be chosen so that the core is not saturated. As evident in Fig. 10(b), the core can saturate in the outer leg where both CM and DM fluxes add. The maximum value of flux $\phi_{O(\max)} = B_{O(max)}A_o$ in the outer core limb must satisfy the following criteria

$$\phi_{O(max)} < B_{Sat}A_o \tag{44}$$

A_o is the cross sectional area of the limb [19]. The maximum flux $\phi_{O(max)}$ comprises CM and DM flux components (45).

$$\phi_{O(max)} = \phi_{CM(max)} + \phi_{DM(max)} \tag{45}$$

$$\phi_{CM(max)} = \frac{N_2}{R_c + R_g + 0.5R_o}\underbrace{\left(\frac{P_{in}}{2V_{in}} + \frac{\Delta i_{CM}}{2}\right)}_{i_{CM(max)}} \tag{46}$$

$$\phi_{DM(max)} = \frac{2N_1}{R_o} i_{DM(max)} = \frac{2N_1}{R_o}\left(\frac{\Delta i_{DM}}{2}\right) \tag{47}$$

The expressions for ripple quantities $\Delta i_{CM}(t)$ and $\Delta i_{DM}(t)$ differ for $D < 0.5$ and $D > 0.5$, resulting in two different expressions for $\phi_{O(max)}$ (48)–(49). Fig. 13 shows the symbolic variation of $\phi_{CM(max)}$ and $\phi_{DM(max)}$. The DM flux increases exponentially for $D < 0.5$ and becomes constant for $D > 0.5$. On the other hand, the CM flux variation with D shows a skewed bell shape for $D < 0.5$ and increases linearly with D for $D > 0.5$.

1) $D < 0.5$:

$$\phi_{O(max)} = \underbrace{\frac{V_{in}D}{4(1-D)fN_1}}_{\phi_{DM(max)}} + \underbrace{\frac{P_{in}L_{cm}}{2V_{in}N_2} + \frac{V_{in}D(1-2D)}{8(1-D)N_2 f}}_{\phi_{CM(max)}} \tag{48}$$

2) $D > 0.5$:

$$\phi_{O(max)} = \underbrace{\frac{V_{in}}{4fN_1}}_{\phi_{DM(max)}} + \underbrace{\frac{P_{in}L_{cm}}{2V_{in}N_2} + \frac{V_{in}(2D-1)}{8N_2 f}}_{\phi_{CM(max)}} \tag{49}$$

$$\frac{\phi_{C(max)}}{\phi_{O(max)}} = \frac{2\phi_{CM(max)}}{\phi_{CM(max)} + \phi_{DM(max)}} \tag{50}$$

In a similar fashion, from Fig. 10(b), the maximum flux in the center leg $\phi_{C(max)}$ is twice CM flux component in the outer leg (46). For intuitive comparison, $\phi_{C(max)}$ can be normalized with $\phi_{O(max)}$ (52). The variation of normalized $\phi_{C(max)}$ with $\gamma = \phi_{DM(max)}/\phi_{CM(max)}$ is plotted in Fig. 14. For $\gamma \leq 1$, the normalized center leg flux exceeds 1 while it drops drastically for $\gamma > 1$.

D. Extension to Multi-Phase Boost Converters

The inverse coupled inductor approach is extendable to even-order $2n$ ($n = 1, 2, 3, 4\ldots$) phase interleaved boost converters to achieve lower input current ripple. The reduction in input current ripple is also beneficial in shrinking the size of the EMI filter due to reduction in DM noise as concluded in [1]. With $2n$-channels, the effective switching frequency is $2nf$. For $n > 1$, an $2n$-channel interleaved boost converter can be considered as

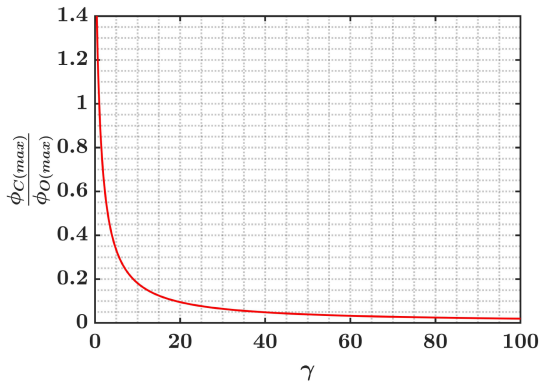

Fig. 14. Normalized center limb maximum flux variation with $\gamma = \phi_{DM(max)}/\phi_{CM(max)}$.

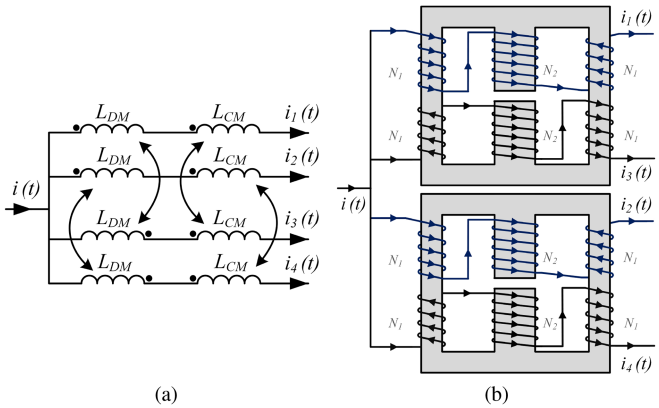

Fig. 15. Magnetics for four-channel interleaved boost converter with inverse couple inductor. (a) L_{CM} and L_{DM}. (b) Proposed IMS.

n two phase interleaved boost converters in Fig. 2, with coupling between alternate channels. For instance, Fig. 15 shows magnetics for a four-phase interleaved boost converter with cascaded L_{CM} and L_{DM} configuration (Fig. 5). The alternate phases 1,3 and 2,4 form 2 two-channel interleaved boost converters. The total number of magnetic cores are 4, same as for the uncoupled case. However, the same four-phase interleaved converter can also be implemented using two proposed IMSs, reducing the total number of magnetic component by half. In general, for a $2n$-phase interleaved converter with inverse coupled inductor, n IMSs are needed compared with n cores for cascaded L_{CM} and L_{DM} configuration (Fig. 5).

For a multi-phase boost converter with the proposed IMS, it is desirable to derive a generalized expression for total input current ripple Δi and channel current ripples Δi_k ($k = 1, 2, 3 \ldots 2n$). As shown in Fig. 15, for a multi-phase boost converter comprising IMSs, coupling only exists between complementary channels, whose currents are 180 °apart. As a result, the channels can be grouped into complementary pairs, forming n two-phase interleaved boost converters. Hence, Δi_k can be computed using (14) and (18).

However, the expressions for Δi in (13) and (17) are not valid for a $2n$-phase boost converter with IMS. The expression for

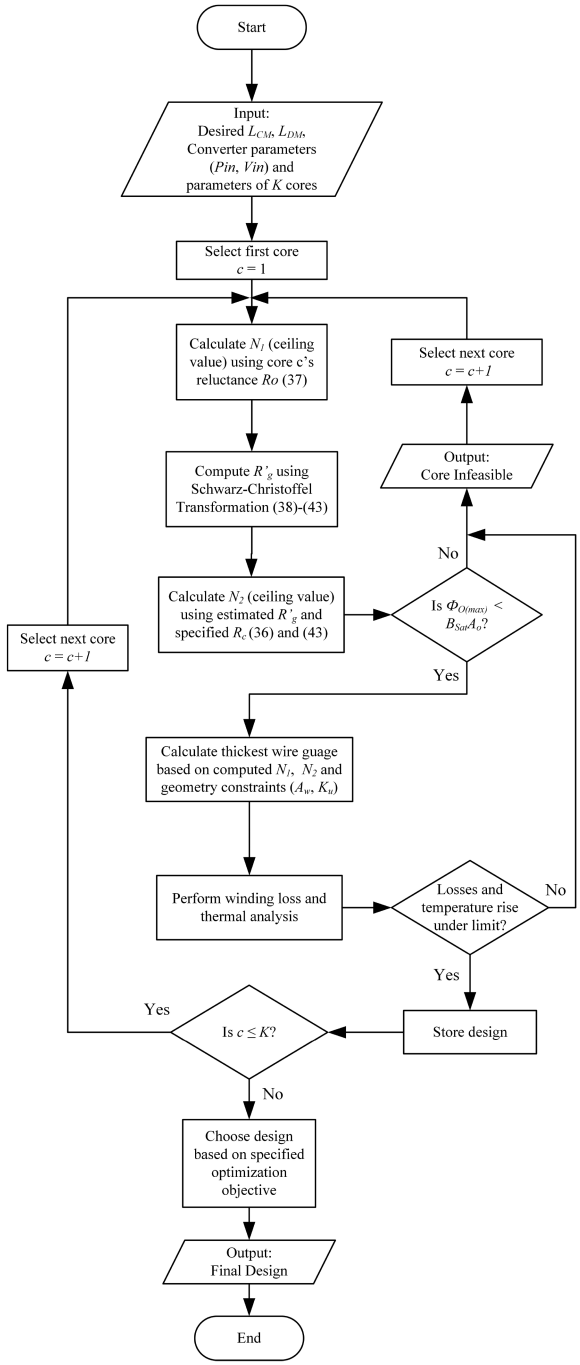

Fig. 16. Proposed design flowchart for integrated magnetic structure.

Δi changes with D. For instance, for $n = 1$ (two-phase), there are two operating regions ($D < 0.5$ and $D > 0.5$), resulting in two different expressions for Δi. The number of regions increases to four ($D < 0.25$, $< 0.25D < 0.5$, $< 0.5D < 0.75$ and, $D > 0.75$) for $n = 2$ (four-phase), leading to four different expressions of Δi. The input current is the sum of CM currents of all $2n$ channels with effective switching frequency $2nf$ and duty cycle D_n expressed as

$$D_n = 2nD - \lfloor 2nD \rfloor \tag{51}$$

A closed-form expression for Δi, incorporating $2nf$ and D_n, for a $2n$-phase boost converter with symmetric coupling between all phase inductors is derived using Lunze's transformation in [28]. For an IMS-based multi-phase boost converter, coupling only exists between complementary channels. Hence, the generalized closed-form expression for Δi needs to be derived by setting the coupling terms for non-complimentary channels to zero in the model derived in [28]. The resulting expression for Δi for an IMS-based $2n$-phase boost converter is

$$\Delta i = \frac{V_{in} D_n (1 - D_n)}{4 L_{CM} (1 - D) nf} \tag{52}$$

V. Proposed IMS Concept Validation

The design of the proposed IMS involves estimation of N_1 and N_2, while ensuring that the air-gap, outer leg maximum flux constraints and thermal constraints are met. Hence, a systematic and holistic approach needs to be devised [21].

A. Design Procedure

Fig. 16 shows the flowchart proposed for designing the IMS. The design process starts with the initialization of converter parameters such as P_{in}, V_{in}, V_{out}, nominal duty cycle D_{nom}, maximum duty cycle D_{max} and required values of L_{CM} and L_{DM}, computed using (11)–(18). D_{nom} refers to duty cycle calculated from the nominal input voltage, whereas D_{max} implies the maximum duty cycle the converter might be operated to regulate the output voltage. A database of K core candidates is also passed as input during the initialization phase.

Passing the initialization phase, a core is then chosen and N_1 turns are calculated using given core outer leg reluctance R_o. This is followed by the estimation of air-gap reluctance R'_g using the Schwarz-Christoffel transformation procedure (38)–(43), discussed in the previous section. The corrected R'_g is then used to compute the value of N_2 using the specified value of L_{CM}. After N_1 and N_2 have been estimated, the maximum outer leg flux constraint (44) needs to be checked. According to (48) and (49), $\phi_{O(max)}$ differs for $D < 0.5$ and $D > 0.5$. Further, it reaches the maximum value for $D = 1$. If specified D_{max} is not equal to 1, then $\phi_{O(max)}$ at $D = D_{max}$ is used to verify (44), else maximum value of $\phi_{O(max)}$ at $D = 1$ is used. If the constraint is not met, the process stops, initializes the next core and redirects to the computation of N_1. If constraint is met, the process moves forward with wire gauge selection and loss analysis.

The wire gauge selection is performed based on the available window area A_w and desirable window utilization factor K_u. The optimal selection of K_u depends on voltage insulation and cooling requirements. High K_u implies close proximity of windings, which hampers heat exchange and is a potential cause for high inter-winding parasitic capacitance [19]. If the calculated wire thickness is enough to keep losses and temperature rise under the desired limit, the design is concluded as feasible and is stored. The following core in the database is then loaded and the design procedure is repeated till all cores are traversed. Finally, an optimal design can be chosen from the stored feasible designs based on the desired goal, such as size, cost and power density.

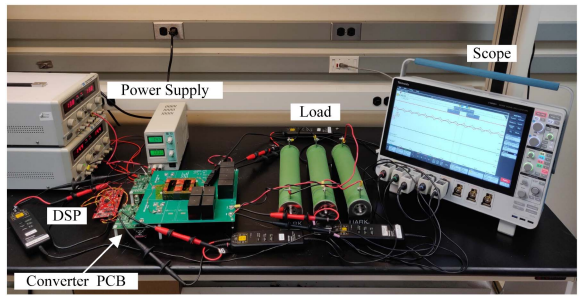

Fig. 17. Experimental setup.

TABLE I
Converter Specifications

Parameter	Value
V_{in}	100 V
V_{out}	168 V
P_{in}	300 W
D_{nom}	0.41
D_{max}	0.45
f	70 kHz
Δi	0.60 A
$\Delta i_1 = \Delta i_2$	0.60 A
L_{CM}	155 uH
L_{DM}	806 uH

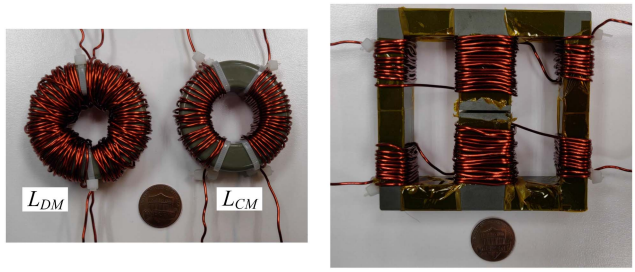

(a) (b)

Fig. 18. Developed prototypes. (a) Prototype 1 (IMS). (b) Prototype 2.

B. Experimental Setup and Inductor Prototype Design

To verify and compare the effectiveness of proposed IMS with cascaded inverse (DM) and direct coupled (CM) inductor implementation, a low-power converter test bench is developed (Fig. 17). The phase-legs are built using two Half-Bridge SiC-based KIT-CRD-8FF65P evaluation board from CREE. The gating signals are generated using Texas Instrument LAUNCHXL-F28379D DSP. Table I summarizes the converter specifications.

For converter magnetics, two inductor prototypes are developed (Fig. 18). The first prototype (Prototype 1) is based on the proposed integrated structure. It is built using B66375G0500X187 E-core from TDK, with an air-gap of 1 mm in the center leg. The core is composed of N87 ferrite material

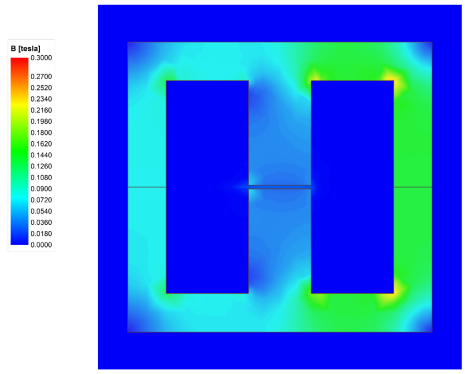

Fig. 19. FEA result for maximum limb flux $\phi_{O(max)}$.

TABLE II
DEVELOPED INDUCTOR PROTOTYPES COMPARISON

Parameter	Value		
	Prototype 1	Prototype 2	
		CM	DM
Core Manufacturer	TDK	Magnetics	
Core Model	E-Core (B66375G0500X187)	Toroid (C058438A2)	
Number of Turns	N_1 = 10, N_2 = 16	23	53
L_{CM} (μH)	155	151	-
L_{DM} (μH)	801	-	795
Wire Guage	18 AWG		
Copper Loss (mW)	340	200	510
Core Loss (mW)	5710	870	1436
Weight (g)	380	220	300
Volume (cm^3)	124	40.5	40.5
Cost $(\$)$	32	26	26

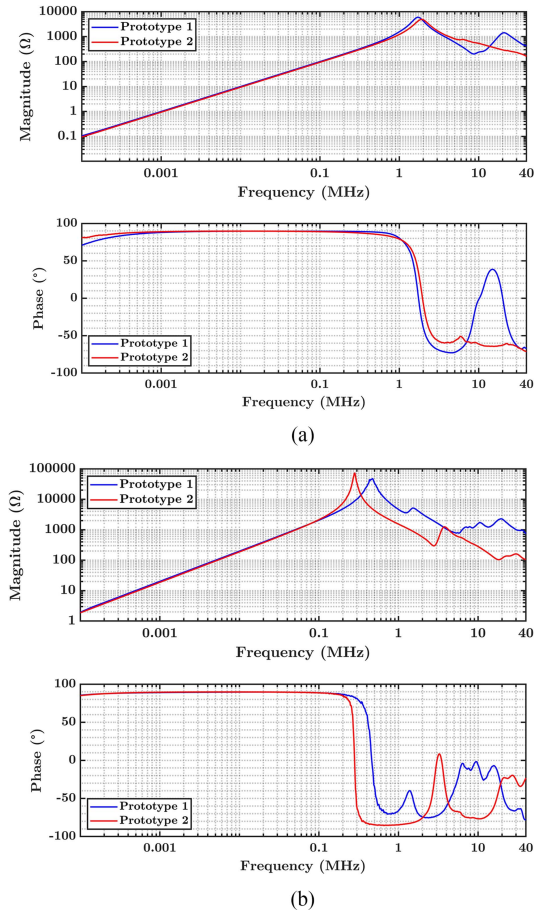

Fig. 20. Impedance comparison of both prototypes. (a) CM. (b) DM.

with saturation flux density B_{Sat} of 490 mT at 25 °C. The second prototype (Prototype 2) is built for benchmarking, using two separate High Flux (HF) toroids from Magnetics. The toroids are wound using the direct-winding approach to lower parasitic capacitance [29]. The design procedure discussed in the previous subsection is followed for the integrated structure. The design is further validated through a coupled-transient simulation of the converter in ANSYS Twin Builder. The IMS prototype is drawn and developed in ANSYS Maxwell 3D using the transient solver. The 3D magnetic structure is linked to the electric circuit in Twin Builder. Fig. 19 shows the magnetic field density B at the instant where the limb flux is maximum in the right outer limb. The maximum magnetic field density is below the saturation value and aligns with the calculated 181 mT.

Table II tabulates the design parameters and measured inductances of both prototypes. Due to the high permeability of N87 material, the number of turns N_1 and N_2 for the proposed IMS prototype are lower than prototype 2 inductors (L_{CM} and L_{DM}). This results in 52 % and 27 % reduction in total copper losses and weight, respectively. The core losses for IMS prototype 1 are higher due to N87 material composition. However, it shall be noted that for the IMS prototype, the core selection is based on availability from the vendor and is for concept demonstration purposes. To increase core utilization and reduce core losses, a custom-sized core using advanced materials with high permeability, such as nano-crystalline, can be fabricated.

The conductor size selected for the winding is AWG 18. This gives plenty of space for winding for both prototypes. For prototype 1, the gap between core and winding at the air-gap is approximately 36 mm, which is greater than twice the air-gap length. Hence, the fringing losses at air-gap are negligible and can be ignored according to [24], [30], [31], [32].

C. Impedance Measurements

The values of L_{CM} and L_{DM} for both prototypes are measured using the Bode 100 Network Analyzer. For measuring L_{CM}, the two winding terminals on each side are shorted and the impedance analyzer is connected across them. Assuming perfect coupling, the measured value is L_{CM}. Similarly, L_{DM} is measured by shorting winding terminals of one side only connecting the other side to the network analyzer; the inductance measured is $4L_{DM}$. Fig. 20(a) and 20(b) compare the CM and DM impedance measurement results. The CM impedance of both prototypes nearly follows each other. However, for DM impedance measurement, prototype 2 has a lower self-resonant frequency (more EPC) than IMS prototype 1. This is because the DM inductor for prototype 2 has more turns to achieve the

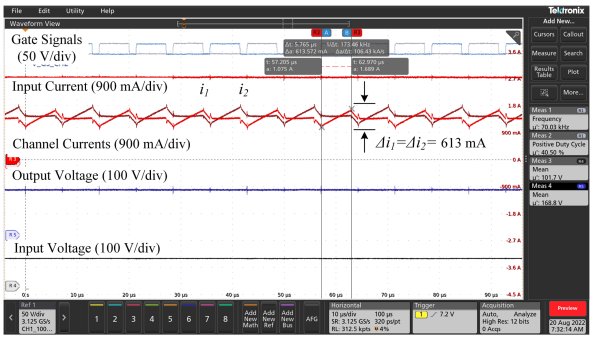

(a)

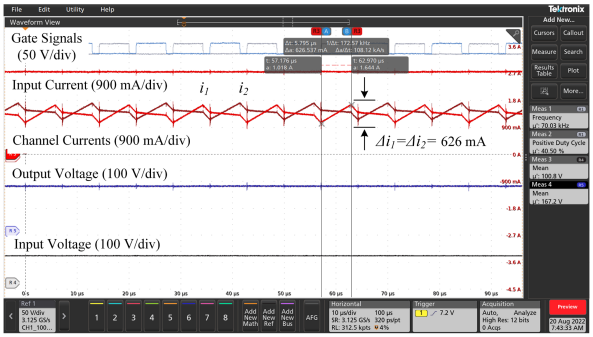

(b)

Fig. 21. Test Results. (a) Prototype 1 (IMS). (b) Prototype 2.

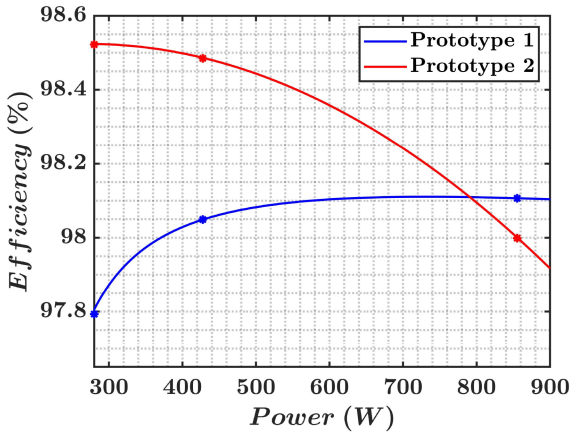

Fig. 22. Efficiency comparison for both prototypes.

same L_{DM} (2.5 times), compared with prototype 1, leading to higher EPC [29], [33], [34], [35], [36].

D. Experimental Results

The impedance measurement procedure is followed by hardware test of prototypes on the developed test bench. The measured waveforms for both cases are presented in Fig. 21. The channel current ripples Δi_1 and Δi_2 for both prototypes is approximately 0.6 A as designed. However, compared with prototype 1, having lower EPC, the channel currents for prototype 2 have capacitive current spikes during switching transition due to higher EPC, substantiating effectiveness of the proposed structure.

TABLE III
SLOPE EXPRESSIONS

Slope	Expression	
	$D < 0.5$	$D > 0.5$
m_{CM1}	$\frac{\Delta i_{CM}}{DT}$	$\frac{\Delta i_{CM}}{(0.5-D)T}$
m_{CM2}	$-\frac{\Delta i_{CM}}{(0.5-D)T}$	$-\frac{\Delta i_{CM}}{(1-D)T}$
m_{DM1}	$\frac{\Delta i_{DM}}{DT}$	$\frac{\Delta i_{DM}}{(1-D)T}$

Fig. 22 compares the efficiency for both prototypes. Curve fitting is performed using the measured efficiency points to establish the efficiency trend for the intermediate power values. According to the results, IMS prototype 1 offers lower efficiency than prototype 2 for power $< 800W$. The lower efficiency is justified because the N87 core material used for concept validation of the proposed IMS concept has a higher core loss than the High Flux material used for prototype 2. Replacing N87 with low loss core material such nano-crystalline could help to increase the light load efficiency. However, for power $> 800W$, the efficiency of the IMS prototype is higher than that of prototype 2. The increase in efficiency can be explained by the substantial increase in copper losses of prototype 2 at high power. Prototype 2 has more turns and channel resistance than prototype 1 (Table II). Since copper losses are proportional to the square of the channel current, the substantial increase in copper losses leads to a significant drop in efficiency for higher power values.

VI. CONCLUSION

Inverse coupling between channel inductors in a two-channel interleaved boost converter is beneficial for lowering channel current ripple and harmonic content. The leakage inductance of the inverse coupled inductor determines the input current ripple, which is CM in both channels, while mutual inductance controls the circulating DM current between channels. Further, the inverse coupled inductor is realized using a cascade of CM and DM coupled inductors for decoupling input and channel current. This approach allows for the specified amount of input and channel current ripple. However, the overall size and count of the magnetic cores are increased. This paper proposes that the miniaturization of magnetics can be achieved by combining both CM and DM inductances in a single structure. A gapped EE core-based IMS design is presented that combines both CM and DM inductances in a single magnetic core structure. The CM and DM inductances are independent and depend on separate winding turns. A prototype is designed, simulated and tested to validate the proposed concept. According to impedance measurement and test results, the IMS prototype offers lower EPC, resulting in cleaner current waveforms than the prototype with separate CM and DM coupled inductors.

APPENDIX A
DERIVATION OF CM AND DM CURRENT FOURIER SERIES

The fourier series of periodic signal $g(t)$ with period T in a single sinusoid form can be be expressed as

$$g(t) = A_0 + \sum_{n=1}^{\infty} A_n cos(n\omega t + \Phi_n) \tag{53}$$

where

$$\begin{aligned} A_0 &= a_o \\ A_n &= \sqrt{a_n^2 + b_n^2} \\ \Phi_n &= tan^{-1}\left(\frac{-b_n}{a_n}\right) \end{aligned} \tag{54}$$

The coefficients a_0, a_n and b_n come from the general fourier series expressions containing sine and cosine terms. The coefficients are related to $g(t)$ as follows

$$\begin{aligned} a_o &= \frac{1}{T}\int_0^T g(t)\,dt \\ a_n &= \frac{2}{T}\int_0^T g(t)cos(n\omega t)\,dt \\ b_n &= \frac{2}{T}\int_0^T g(\tau)sin(n\omega t)\,dt \end{aligned} \tag{55}$$

The CM and DM current waveforms for both uncoupled (Fig. 3) and inverse coupled (Fig. 4) have the same shape but they differ in amplitude and slope, governed by (3)–(18). Hence, to simplify the analysis, the fourier series expansions for $i_{CM}(t)$ and $i_{DM}(t)$ can be first derived in general form with slopes during each interval denoted by m_{CMi} and m_{DMi}. The slopes differ for $D < 0.5$ and $D > 0.5$ and are expressed in terms of CM and DM ripples (Table III), which in turn differ for both uncoupled and inverse coupled configurations. Moreover, it is evident from the waveforms that $i_{CM}(t)$ has a DC component I_{DC}, which is half of the converter input current DC component. Hence, $a_{0CM} = I_{DC}$ for $i_{CM}(t)$ fourier series. DM current is purely AC with zero offset, implying $a_{0DM} = 0$ for $i_{DM}(t)$ fourier series.

By using the expressions for slopes in Table III and ripples currents (3)–(18) and solving (54)–(55) for converter waveforms, following expressions for A_{nCM} and A_{nDM} are obtained for both inductor configurations

A. Uncoupled

$$A_{nCM(uc)} = \frac{2V_{in}}{L}\left(\sqrt{\frac{1 - cos(2n\pi(2D-1))}{512n^4\pi^4 f^2 (D-1)^2}}\right) \tag{56}$$

$$A_{nDM(uc)} = \frac{4V_{in}}{L}\left(\sqrt{\frac{(cos(2n\pi D) - 1)(cos(n\pi) - 1)}{64n^4\pi^4 f^2 (D-1)^2}}\right) \tag{57}$$

B. Inverse Coupled

$$A_{nCM(ic)} = \frac{V_{in}}{L_{CM}}\left(\sqrt{\frac{1 - cos(2n\pi(2D-1))}{512n^4\pi^4 f^2 (D-1)^2}}\right) \tag{58}$$

$$A_{nDM(ic)} = \frac{2V_{in}}{L_{DM}}\left(\sqrt{\frac{(cos(2n\pi D) - 1)(cos(n\pi) - 1)}{64n^4\pi^4 f^2 (D-1)^2}}\right) \tag{59}$$

The square root terms for both CM and DM coefficients (56)–(58) are identical for both uncoupled and inverse coupled configurations. For simplification, these terms can be represented as amplitude scaling functions $g(D, f, n)$ and $h(D, f, n)$ for CM and DM coefficients respectively, as shown in (20)–(22).

$$g(D, f, n) = \sqrt{\frac{1 - cos(2n\pi(2D-1))}{512n^4\pi^4 f^2 (D-1)^2}}$$

$$h(D, f, n) = \sqrt{\frac{(cos(2n\pi D) - 1)(cos(n\pi) - 1)}{64n^4\pi^4 f^2 (D-1)^2}}$$

APPENDIX B
DERIVATION POWER SEMICONDUCTOR LOSS

A. Switching Loss P_{sw}

The normalized switching loss ratio $P_{sw(ic)b,t}/P_{sw(uc)b,t}$ for the bottom and top device using (24) and (26) and $\zeta = T_{ON}/T_{OFF}$ can be expressed as

$$\frac{P_{sw(ic)b}}{P_{sw(uc)b}} = \frac{(I_{DC} - \Delta i_{1,2(ic)})\zeta + (I_{DC} + \Delta i_{1,2(ic)})}{(I_{DC} - \Delta i_{1,2(uc)})\zeta + (I_{DC} + \Delta i_{1,2(uc)})} \tag{60}$$

$$\frac{P_{sw(ic)t}}{P_{sw(uc)t}} = \frac{(I_{DC} + \Delta i_{1,2(ic)})\zeta + (I_{DC} - \Delta i_{1,2(ic)})}{(I_{DC} + \Delta i_{1,2(uc)})\zeta + (I_{DC} - \Delta i_{1,2(uc)})} \tag{61}$$

For equal input current ripple Δi ($L = 2L_{CM}$ for uncoupled), the above expressions reduce to a function $M_{b,t}(D, \alpha, \zeta, \kappa)$ for both $D < 0.5$ and $D > 0.5$ by substituting ripple current expressions and by taking $\Delta i_{1,2(uc)} = \kappa I_{DC}$ (62)–(65) shown at the top of next page.

B. Conduction Loss P_{co}

The conduction loss P_o primarily depends on the DC component of the current flowing through both top and bottom devices during converter operation. The bottom device conducts during current-ramp up interval, where the inductor stores energy. The top device conducts during the discharging interval, where stored energy in inductor is delivered to the output capacitor and load.

The general expression for conduction losses (25)–(27), involve finding the RMS value of the device current. The device current contains ripple and DC (I_{DC}) components. Compared with uncoupled inductor, the inverse coupled configuration only impacts the channel ripple current component. Hence, minor reduction in conduction loss is expected with the inverse coupled implementation. This can be visualized through the conduction loss ratio $P_{co(ic)b,t}/P_{co(uc)b,t}$, denoted as $N_{b,t}(D, \alpha, \kappa)$, which

Switching Loss $D < 0.5$:

$$M_b(D,\alpha,\zeta,\kappa) = \frac{2\zeta(2+D(\kappa-2)+2\kappa(1-D-\zeta)+4(1-D)+\kappa\alpha(1-\zeta)}{2\zeta(2+D(\kappa-2)+2\kappa(1-D-\zeta)+4(1-D)} \tag{62}$$

$$M_t(D,\alpha,\zeta,\kappa) = \frac{2\zeta(D(\kappa+2)-2)+2\kappa(1-D-\zeta)-4(1-d)+\kappa\alpha(1-\zeta)}{2\zeta(D(\kappa+2)-2)+2\kappa(1-D-\zeta)-4(1-d)} \tag{63}$$

Switching Loss $D > 0.5$:

$$M_b(D,\alpha,\zeta,\kappa) = \frac{\kappa(1-\zeta)+2D(\kappa(\zeta-1)-2D(1+\zeta))+\kappa\alpha(\zeta-1)}{2D(\kappa(\zeta-1)-2D(1+\zeta))} \tag{64}$$

$$M_t(D,\alpha,\zeta,\kappa) = \frac{\kappa(1-\zeta)+2D(\kappa(\zeta-1)+2D(1+\zeta))+\kappa\alpha(\zeta-1)}{2D(\kappa(\zeta-1)+2D(1+\zeta))} \tag{65}$$

Conduction Loss $D < 0.5$:

$$N_b(D,\alpha,\kappa) = \frac{D^2(4\kappa^2+48)+D(-4\kappa^2-96)+\kappa^2(1+\alpha^2+2\alpha(1-2D))+48}{4(\kappa^2+12)(D-1)^2} \tag{68}$$

$$N_t(D,\alpha,\kappa) = \frac{D^3(4\kappa^2+48)-D^2(8\kappa^2+144)+D(5\kappa^2+144)+\kappa^2(2\alpha D(1-2D)+\alpha^2(5D-3)-1)-48}{4(\kappa^2+12)(D-1)^3} \tag{69}$$

Conduction Loss $D > 0.5$:

$$N_b(D,\alpha,\kappa) = \frac{D^3(4\kappa^2+48)-4\kappa^2D^2+\kappa^2D+(\alpha^2(5D-2)+\alpha\kappa^2(4D^2-6D)+2\alpha)}{4D^3(\kappa^2+12)} \tag{70}$$

$$N_t(D,\alpha,\kappa) = \frac{\kappa^2(4D^2-4D+1+\alpha^2-2\alpha(1-2D))+48D^2}{4D^2(\kappa^2+12)} \tag{71}$$

simply reduces to the ratio of device RMS current for both devices as follows

$$\frac{P_{co(ic)b}}{P_{co(uc)b}} = N_b(D,\alpha,\kappa) = \frac{\int_0^{DT} i_{1,2(ic)}^2(\tau)\,d\tau}{\int_0^{DT} i_{1,2(uc)}^2(\tau)\,d\tau} \tag{66}$$

$$\frac{P_{co(ic)b}}{P_{co(uc)b}} = N_t(D,\alpha,\kappa) = \frac{\int_{DT}^{T} i_{1,2(ic)}^2(\tau)\,d\tau}{\int_{DT}^{T} i_{1,2(uc)}^2(\tau)\,d\tau} \tag{67}$$

Solution of integrals in (67)–(66) according to converter waveforms in Figs. 3 and 4 with equal input current ripple Δi ($L = 2L_{CM}$ for uncoupled configuration), yields the closed-form expressions (68)–(71) shown at the top of this page, for $N_{b,t}(D,\alpha,\kappa)$ for both top and bottom devices.

REFERENCES

[1] C. Wang, "Investigation on interleaved boost converters and applications," Ph.D. dissertation, Fac. Virginia Polytechnic Inst., Virginia Tech, 2009.

[2] M. Muhammad, M. Armstrong, and M. A. Elgendy, "A nonisolated interleaved boost converter for high-voltage gain applications," *IEEE Trans. Emerg. Sel. Topics Power Electron.*, vol. 4, no. 2, pp. 352–362, Jun. 2016.

[3] F. Zhu and Q. Li, "Coupled inductors with an adaptive coupling coefficient for multiphase voltage regulators," *IEEE Trans. Power Electron.*, vol. 38, no. 1, pp. 739–749, Jan. 2023.

[4] T. Kang, A. Gandomkar, J. Lee, and Y. Suh, "Design of optimized coupling factor for minimum inductor current ripple in DC-DC converter using multiwinding coupled inductor," *IEEE Trans. Ind. Appl.*, vol. 57, no. 4, pp. 3978–3989, Jul./Aug. 2021.

[5] F. Li, Y. Yao, Z. Wang, and H. Liu, "Coupled-inductor-inverse high step-up converter," *IET Power Electron.*, vol. 11, no. 5, pp. 902–911, 2018.

[6] M. Xu, Y. Dong, and F. C. Lee, "Multiphase voltage regulator having coupled inductors with reduced winding resistance," U.S. Patent US7649434B2, Jan.19, 2010.

[7] Y. Yang, T. Guan, S. Zhang, W. Jiang, and W. Huang, "More symmetric four-phase inverse coupled inductor for low current ripples & high-efficiency interleaved bidirectional buck/boost converter," *IEEE Trans. Power Electron.*, vol. 33, no. 3, pp. 1952–1966, Mar. 2018.

[8] R. Bosshard and J. W. Kolar, "All-SiC 9.5 kW/dm3 on-board power electronics for 50 kW/85 kHz automotive IPT system," *IEEE Trans. Emerg. Sel. Topics Power Electron.*, vol. 5, no. 1, pp. 419–431, Mar. 2017.

[9] P.-L. Wong, P. Xu, P. Yang, and F. Lee, "Performance improvements of interleaving VRMs with coupling inductors," *IEEE Trans. Power Electron.*, vol. 16, no. 4, pp. 499–507, Jul. 2001.

[10] W. Chen, F. Lee, X. Zhou, and P. Xu, "Integrated planar inductor scheme for multi-module interleaved quasi-square-wave (QSW) DC/DC converter," in *Proc. IEEE 30th Annu. Power Electron. Specialists Conf. Rec.*, 1999, pp. 759–762.

[11] F. Yang, X. Ruan, Y. Yang, and Z. Ye, "Interleaved critical current mode boost PFC converter with coupled inductor," *IEEE Trans. Power Electron.*, vol. 26, no. 9, pp. 2404–2413, Sep. 2011.

[12] J. Imaoka and M. Yamamoto, "A novel integrated magnetic structure suitable for transformer-linked interleaved boost chopper circuit," in *Proc. IEEE Energy Convers. Congr. Expo.*, 2012, pp. 3279–3284.

[13] K. J. Hartnett, J. G. Hayes, M. G. Egan, and M. S. Rylko, "CCTT-core split-winding integrated magnetic for high-power DC–DC converters," *IEEE Trans. Power Electron.*, vol. 28, no. 11, pp. 4970–4984, Nov. 2013.
[14] R. Lai, Y. Maillet, F. Wang, S. Wang, R. Burgos, and D. Boroyevich, "An integrated EMI choke for differential-mode and common-mode noise suppression," *IEEE Trans. Power Electron.*, vol. 25, no. 3, pp. 539–544, Mar. 2010.
[15] Y. Chu, S. Wang, N. Zhang, and D. Fu, "A common mode inductor with external magnetic field immunity, low-magnetic field emission, and high-differential mode inductance," *IEEE Trans. Power Electron.*, vol. 30, no. 12, pp. 6684–6694, Dec. 2015.
[16] H. Zhang, B. Zhang, and S. Wang, "Integrated common mode and differential mode inductors with low near magnetic field emission," in *Proc. IEEE Energy Convers. Congr. Expo.*, 2017, pp. 5375–5382.
[17] S. Jiang, Y. Liu, J. Peng, and H. Jiang, "Magnetic integration of EMI filter for grid-connected voltage-source inverters," in *Proc. IEEE 10th Int. Conf. Power Electron. ECCE Asia*, 2019, pp. 917–922.
[18] A. B. Mirza, A. I. Emon, S. S. Vala, and F. Luo, "An integrated magnetic structure for bi-directional two-channel interleaved boost converter with coupled inductor," in *Proc. IEEE Energy Convers. Congr. Expo.*, 2021, pp. 5466–5470.
[19] R. W. Erickson and D. Maksimovic, *Fundamentals of Power Electronics*, 2nd ed. Berlin, Germany: Springer, 2001.
[20] A. Balakrishnan, W. Joines, and T. Wilson, "Air-gap reluctance and inductance calculations for magnetic circuits using a Schwarz-Christoffel transformation," *IEEE Trans. Power Electron.*, vol. 12, no. 4, pp. 654–663, Jul. 1997.
[21] Z. Yang, H. Suryanarayana, and F. Wang, "An improved design method for gapped inductors considering fringing effect," in *Proc. IEEE Appl. Power Electron. Conf. Expo.*, 2019, pp. 1250–1256.
[22] C. W. T. McLyman, *Transformer and Inductor Design Handbook*. Boca Raton, FL, USA: CRC Press, 2017.
[23] H. Liao and J.-F. Chen, "Design process of high-frequency inductor with multiple air-gaps in the dimensional limitation," *J. Eng.*, vol. 2022, no. 1, pp. 16–33, 2022. [Online]. Available: https://ietresearch.onlinelibrary.wiley.com/doi/abs/10.1049/tje2.12087
[24] P. Winkler and W. Guenther, "Using powder materials to replace air-gaps for fringing flux reduction," in *Proc. IEEE Int. Exhib. Conf. Power Electronics, Intell. Motion, Renew. Energy Energy Manage.*, 2017, pp. 1–6.
[25] M. K. Kazimierczuk, *High-Frequency Magnetic Components*. Hoboken, NJ, USA: Wiley, 2014.
[26] W. G. Hurley and W. H. Wölfle, *Transformers and Inductors for Power Electronics: Theory, Design and Applications*. Hoboken, NJ, USA: Wiley, 2014.
[27] J. Muhlethaler, J. W. Kolar, and A. Ecklebe, "A novel approach for 3D air gap reluctance calculations," in *Proc. IEEE 8th Int. Conf. Power Electron.*, 2011, pp. 446–452.
[28] H.-B. Shin, "Generalised steady-state analysis of multiphase interleaved boost converter with coupled inductors," *IEE Proc. - Electric Power Appl.*, vol. 152, no. 10, pp. 584–594, May 2005.
[29] B. Liu, R. Ren, F. Wang, D. Costinett, and Z. Zhang, "Winding scheme with fractional layer for differential-mode toroidal inductor," *IEEE Trans. Ind. Electron.*, vol. 67, no. 2, pp. 1592–1604, Feb. 2020.
[30] W. A. Roshen, "Fringing field formulas and winding loss due to an air gap," *IEEE Trans. Magn.*, vol. 43, no. 8, pp. 3387–3394, Aug. 2007.
[31] P. Wallmeier, "Improved analytical modeling of conductive losses in gapped high-frequency inductors," *IEEE Trans. Ind. Appl.*, vol. 37, no. 4, pp. 1045–1054, Jul. 2001.
[32] W. Chen, X. Huang, and J. Zheng, "Improved winding loss theoratical calculation of magnetic component with air-gap," in *Proc. IEEE 7th Int. Power Electron. Motion Control Conf.*, 2012, pp. 471–475.
[33] S. W. Pasko, M. K. Kazimierczuk, and B. Grzesik, "Self-capacitance of coupled toroidal inductors for EMI filters," *IEEE Trans. Electromagn. Compat.*, vol. 57, no. 2, pp. 216–223, Apr. 2015.
[34] A. Massarini and M. Kazimierczuk, "Self-capacitance of inductors," *IEEE Trans. Power Electron.*, vol. 12, no. 4, pp. 671–676, Jul. 1997.
[35] T. Neugebauer and D. Perreault, "Parasitic capacitance cancellation in filter inductors," in *Proc. IEEE 35th Annu. Power Electron. Specialists Conf.*, 2004, pp. 3102–3107.
[36] R. A. G. Jimenez, G. G. Oggier, D. P. Fernandez, and J. C. Balda, "Analysis of current resonances due to winding parasitic capacitances in medium-voltage medium-frequency transformers," in *Proc. IEEE Appl. Power Electron. Conf. Expo.*, 2022, pp. 939–943.

Abdul Basit Mirza (Graduate Student Member, IEEE) received the bachelor's degree (Hons.) in electrical engineering (power) from the University of Engineering and Technology, Lahore, Pakistan, in 2018 the master's degree in 2022 from Stony Brook University, Stony Brook, NY, USA, concentrating on MVDC breakers using WBG-based power electronics, where he is currently working toward the Ph.D. degree in electrical engineering. He is a graduate research assistant involved in research projects with the Oak Ridge National Laboratory, Oak Ridge, TN, USA, and Federal Aviation Administration. In 2022, he was a research intern at GE Global Research, Niskayuna, NY, USA. His research interests include system-level design of high-density wide band gap (WBG) based power converters and electromagnetic interference and compatibility (EMI/EMC) characterization.

Asif Imran Emon (Graduate Student Member, IEEE) received the B.Sc. degree in electrical and electronic engineering from the Chittagong University of Engineering and Technology, Chittagong, Bangladesh, in 2015, the M.S. degree from the University of Arkansas, Fayetteville, AR, USA, in 2022, and the Ph.D. degree from the State University of New York, Stony Brook, NY, USA, in 2022. He interned with GE Global Research, Niskayuna, NY, during the summer of 2021. In 2022, he was an EMC Design Engineering Team intern with Apple Inc., Cupertino, CA, USA. His research interests include power module packaging of wide band-gap devices, efficient energy conversion and electromagnetic interference, and compatibility analysis in motor drives.

Sama Salehi Vala (Graduate Student Member, IEEE) received the B.Sc. and M.Sc. degrees in electrical engineering from the University of Tabriz, Tabriz, Iran, in 2014 and 2018, respectively. She is currently working toward the Ph.D. degree in electrical engineering with Stony Brook University, Stony Brook, NY, USA. She interned with Rivian, Carson, CA, USA, during the summer of 2022. In 2023, she interned with the Design Engineering Team, Tesla, Palo Alto, CA. Her research interests include design and analysis of power electronics converters, motor drives, high-voltage power module packaging, renewable energy systems, reliability, and partial discharge.

Fang Luo (Senior Member, IEEE) received the bachelor's and Ph.D. degrees from the Huazhong University of Science and Technology, Wuhan, China, and jointly from Virginia Tech, Blacksburg, VA, USA, in 2003 and 2010, respectively. He was an Assistant Professor with the Electrical Engineering Department, University of Arkansas, Fayetteville, AR, USA, from 2017 to 2020, and a Research Assistant Professor with The Ohio State University, Columbus, OH, USA, from 2014 to 2017. He was a Visiting Ph.D. Student from 2007 to 2010 and then a Postdoctoral Researcher from 2010 to 2014 with Virginia Tech. He is currently an Empire Innovation Associate Professor and the Director of the Spellman High Voltage Laboratory, Stony Brook University (SUNY Stony Brook), Stony Brook, NY, USA, with his background in power electronics. His research interests include high-power density converter design, high-density electromagnetic interference (EMI) filter design and integration, and power module packaging/integration for wide bandgap devices. Dr. Luo is a Member of the American Institute of Aeronautics and Astronautics (AIAA) and American Society of Mechanical Engineers (ASME). He was the recipient of the NSF CAREER Award.